SCIENCE CHINA
Information Sciences

• RESEARCH PAPER •

June 2026, Vol. 69, Iss. 6, 160305:1–160305:14
https://doi.org/10.1007/s11432-025-4916-4

Special Topic: Integrated Optical Fiber Communication and Sensing Systems

Optical fiber communication and distributed multi-parameter sensing integrated network for smart power grid applications

Xiaohui TANG[1,2], Yanyang LEI[1,2], Jinglin SUI[1,2], Meng XIA[1], Yaxi YAN[3], Dexin BA[1,2*] & Yongkang DONG[1,2*]

[1]*National Key Laboratory of Laser Spatial Information, Harbin Institute of Technology, Harbin 150001, China*
[2]*Zhengzhou Advanced Research Institute, Harbin Institute of Technology, Zhengzhou 450007, China*
[3]*Photonics Research Institute, Department of Electrical and Electronic Engineering, The Hong Kong Polytechnic University, Hong Kong 999077, China*

Received 11 November 2025/Revised 25 February 2026/Accepted 13 April 2026/Published online 21 May 2026

Abstract Power cables face increasingly complex operational and environmental challenges, requiring integrated multi-parameter monitoring of temperature, strain, and vibration. In this paper, we present a high-capacity integrated sensing and communication over fiber (ISACoF) system for optical transport networks (OTN). The system employs a dual-heterodyne detection architecture combined with a counter-propagation wavelength-division multiplexed ISACoF technology, enabling co-propagation and cooperative demodulation of Brillouin optical time domain reflectometry (BOTDR) and distributed acoustic sensing (DAS) signals within a single optical fiber. This configuration enables simultaneous high-precision monitoring while maintaining 100 Gbit/s polarization-multiplexed quadrature phase-shift key (PM-QPSK) transmission performance. Experimental validation over a 100.977 km fiber link shows an optical signal-to-noise ratio above 23 dB and a bit error rate (BER) on the order of 10^{-7}. The BOTDR subsystem achieves 40 m spatial resolution with 2 MHz frequency shift accuracy, and the DAS subsystem exhibits 0.37 rad phase noise, detecting 1 Hz vibrations. Additionally, the system was able to predict a 10 mm ice layer on a 500 kV line and track temperatures up to 30°C during direct current (DC) de-icing. These results confirm strong compatibility, minimal interference, and high predictive capability, offering a resource-efficient foundation for intelligent and self-healing power OTN infrastructures.

Keywords integrated sensing and communication over fiber, multi-parameter sensing, optical transport networks, Brillouin optical time domain reflectometry, distributed acoustic sensing

Citation Tang X H, Lei Y Y, Sui J L, et al. Optical fiber communication and distributed multi-parameter sensing integrated network for smart power grid applications. Sci China Inf Sci, 2026, 69(6): 160305, https://doi.org/10.1007/s11432-025-4916-4

1 Introduction

With the rapid development of modern power systems and smart grids, power communication networks have emerged as the central nervous system for real-time monitoring, dynamic control, differential protection, and intelligent decision-making [1]. The optical transport network (OTN), which has high reliability, large capacity, and low latency, serves as a cornerstone of backbone power communication [2]. Nevertheless, the long-term integrity of overhead composite cables, such as optical fiber composite overhead ground wires (OPGW), is of utmost importance. Environmental and mechanical factors, including cyclic icing, wind-induced vibrations, temperature fluctuations, and extreme weather conditions, can induce mechanical fatigue, fiber deformation, signal attenuation, and material degradation, thereby compromising the stability and reliability of power systems [3]. Consequently, developing an intelligent monitoring and early-warning framework that can perform long-term, real-time, and high-precision monitoring of overhead cables is crucial for resilient power communication networks.

Distributed fiber optic sensing (DFOS) has emerged as a pivotal technology for monitoring transmission infrastructures, offering long sensing distances, fully distributed measurements, high spatial resolution, and immunity to electromagnetic interference [4, 5]. Among DFOS approaches, Brillouin-based techniques, such as Brillouin optical time domain reflectometry (BOTDR), enable quantitative measurement of distributed strain and temperature along the fiber, facilitate splice identification [6, 7], and support diverse applications including sag monitoring [8],

* Corresponding author (email: dexinba@hit.edu.cn, aldendong@163.com)

icing-load assessment [9], and detection of transient thermal events [10–13]. Rayleigh-scattering-based distributed acoustic sensing (DAS) offers exceptional sensitivity to cable vibrations [14], enabling the detection of aeolian vibrations, modal dynamics, and icing thickness [15, 16]. Brillouin-based sensing offers high measurement accuracy for static strain and temperature distributions; however, it is inherently limited in its ability to capture dynamic variations. In contrast, Rayleigh-based sensing excels at detecting rapid vibrations and transient events but lacks absolute quantitative precision. The synergistic integration of these two sensing modalities facilitates comprehensive monitoring of the thermal, mechanical, and dynamic behaviors of overhead cables. Consequently, hybrid DFOS systems hold significant promise for intelligent diagnostics within power grid infrastructures.

As communication networks evolve toward higher speed and extended coverage, recent surveys have highlighted the growing interest in intelligent integrated sensing and communication systems and their potential in 6G networks, emphasizing the importance of simultaneous sensing and high-capacity data transmission over shared optical infrastructure [17]. At the same time, fiber resources are becoming increasingly scarce. Reserving multiple dedicated fibers for sensing would lead to significant resource wastage. This challenge has led to the development of ISACoF, which enables co-propagation of communication and sensing signals without compromising network performance [18]. Forward transmission-based ISACoF approaches exploit the optical phase or polarization features of communication signals for environmental sensing, offering cost-effective long-range monitoring; however, they suffer from cumulative effects that reduce spatial localization and multi-source disturbance discrimination [19–25]. In contrast, backscatter-based ISACoF schemes, often enabled by wavelength division multiplexing (WDM), enable the coexistence of high-capacity data and distributed sensing with minimal interference, as demonstrated in field trials for vehicle monitoring and environmental sensing [26–29]. Recent advances include integrating ϕ-OTDR probe pulses with high-speed data signals over a single wavelength, achieving long-range, high-precision vibration monitoring while improving transmission performance [25].

Despite these advances, most existing studies focus on single-parameter monitoring or the impact of sensing on communication performance. As a result, single-mechanism approaches cannot achieve multi-parameter monitoring and thus fail to meet the requirements of complex power grid monitoring, with nonlinear crosstalk effects largely underexplored. To address these limitations, this work proposes a 100 Gbit/s OTN ISACoF system that employs dual-heterodyne detection and backward WDM integration, enabling simultaneous BOTDR and DAS sensing in a single fiber. Experimental validation over a 100.997 km link demonstrates high-precision monitoring of temperature, strain, and vibration, with minimal impact on data transmission, confirming the feasibility of deploying intelligent, resilient, and resource-efficient ISACoF systems on existing OTN infrastructures.

The rest of this paper is organized as follows. Section 2 provides an introduction to simultaneous Brillouin and Rayleigh sensing, emphasizing the nonlinear interactions between communication and sensing mechanisms. Section 3 offers a comprehensive description of the ISACoF system design. Section 4 evaluates the sensing capabilities, data transmission efficiency, and overall effectiveness of the system in both co- and counter-propagating ISACoF scenarios, including validation in field applications.

2 Method and system

2.1 Dual-heterodyne scheme for BOTDR and DAS

To achieve simultaneous demodulation of BOTDR and DAS, a dual-heterodyne detection architecture is employed. A narrow-linewidth laser provides continuous-wave (CW) light that is divided into two main branches. One branch simultaneously serves as the probe pulse for BOTDR and as the sensing light for DAS. In contrast, the other branch is split into two reference paths, serving as the Brillouin local oscillator (LO) and the Rayleigh LO, respectively. In the sensing system, an acousto-optic modulator (AOM) generates optical pulses and introduces a frequency shift for heterodyne detection. The probe and reference optical fields can be expressed as

$$E_P(t) = E_P \mathrm{e}^{\mathrm{j}[2\pi(v_0+v_{AOM})t+\varphi_P]}, \tag{1}$$

$$E_{LO,B}(t) = E_{LO,B} \mathrm{e}^{\mathrm{j}[2\pi v_0 t+\varphi_{LO,B}]}, \tag{2}$$

$$E_{LO,R}(t) = E_{LO,R} \mathrm{e}^{\mathrm{j}[2\phi v_0 t+\varphi_{LO,R}]}, \tag{3}$$

where E_P, $E_{LO,B}$, and $E_{LO,R}$ are the amplitudes of the probe, Brillouin LO, and Rayleigh LO, respectively, v_0 is the laser frequency, v_{AOM} is the frequency shift introduced by the AOM, and φ_P, $\varphi_{LO,B}$, and $\varphi_{LO,R}$ are their initial phases.

The total backscattered field in the fiber arises from the combined contributions of Rayleigh backscattering (RBS), as well as Brillouin Stokes and anti-Stokes components.

$$\begin{aligned} E(t) = & E_R e^{j[2\pi(v_0+v_{AOM})t+\varphi_R(t)+\varphi_{R0}]} \\ & + E_{B,S} \mathrm{e}^{\mathrm{j}[2\pi(v_0+v_{AOM}-v_B)t+\varphi_{B,S}(t)+\varphi_{S0}]} \\ & + E_{B,AS} \mathrm{e}^{\mathrm{j}[2\pi(v_0+v_{AOM}+v_B)t+\varphi_{B,AS}(t)+\varphi_{AS0}]}, \end{aligned} \tag{4}$$

where E_R, $E_{B,S}$, and $E_{B,AS}$ are the amplitudes of the Rayleigh, Stokes, and anti-Stokes scattering, respectively, and v_B is the Brillouin frequency shift (BFS). The phase variations of Rayleigh backscattered light, Brillouin Stokes light, and Brillouin anti-Stokes light are denoted by $\varphi_R(t)$, $\varphi_{B,S}(t)$, and $\varphi_{B,AS}(t)$, respectively, while φ_{R0}, φ_{S0}, and φ_{AS0} represent their initial phases. After optical filtering, the Rayleigh and Brillouin scattered components are each mixed with their corresponding local LO signals at a 3 dB coupler. The AC components of the beat signals detected by the photodetectors can be expressed as follows:

$$P_{R,AC}(t) = \Re\sqrt{P_R(t)P_{LO,R}(t)}\cos[2\pi v_{AOM}t + \varphi_R(t) + \varphi_{R0} - \varphi_{LO,P}], \tag{5}$$

$$P_{B,S,AC}(t) = \Re\sqrt{P_{B,S}(t)P_{LO,B}(t)}\cos[2\pi(v_B - v_{AOM})t + \varphi_{B,S}(t) + \varphi_{S0} - \varphi_{LO,B}], \tag{6}$$

where $P_{R,AC}(t)$ and $P_{B,S,AC}(t)$ represent the Rayleigh and Brillouin scattering powers, while the phase terms $\varphi_R(t)$ and $\varphi_{B,S}(t)$ carry the vibration and strain/temperature information, respectively.

2.2 Theoretical analysis of nonlinear effects

The implementation of dense wavelength-division multiplexing (DWDM) in optical fiber transmission systems not only addresses the escalating bandwidth demand but also establishes a unified, scalable platform for the seamless integration of OTN with distributed sensing techniques such as BOTDR and DAS. Nevertheless, such co-transmission inevitably induces complex physical interactions arising from nonlinear coupling between optical fields and the fiber medium, as well as inter-channel crosstalk among co-propagating wavelengths when multiple channels coexist within the same fiber.

In standard single-mode optical fibers, nonlinear optical phenomena are generally categorized into stimulated scattering and Kerr-type effects, which are distinguished by their physical origins [30]. Stimulated scattering involves the transfer of energy between the optical field and the medium, leading to processes such as stimulated Raman scattering (SRS) and stimulated Brillouin scattering (SBS). The Kerr effect arises from the optical intensity dependence of the refractive index, giving rise to self-phase modulation (SPM), cross-phase modulation (XPM), and four-wave mixing (FWM).

The propagation of an optical signal in a fiber can be described by the generalized nonlinear Schrödinger equation (GNLSE) [31,32], expressed as

$$\frac{\partial A}{\partial z} + \frac{\alpha}{2}A + \frac{\mathrm{i}}{2}\beta_2\frac{\partial^2 A}{\partial T^2} - \frac{1}{6}\beta_3\frac{\partial^3 A}{\partial T^3} = \mathrm{i}\gamma|A|^2A + \mathrm{i}\gamma A\left[\frac{\mathrm{i}}{\omega_0}\frac{\partial(|A|^2A)}{\partial T}\right] + \mathrm{i}\gamma\left[-T_R A\frac{\partial(|A|^2)}{\partial T}\right] + g_B Q(z,T)A. \tag{7}$$

Eq. (7) describes the nonlinear differential equation governing the evolution of the complex optical field envelope $A(z,T)$ during propagation along an optical fiber. Here, $\omega_0 = 2\pi f_0$ represents the angular frequency of the optical carrier, used for normalizing the self-steepening term, z denotes the longitudinal propagation distance, and T represents the retarded time in a reference frame moving at the group velocity. The parameters α, β_2, β_3, and γ correspond to the fiber attenuation coefficient, group-velocity dispersion (GVD) parameter, third-order dispersion (TOD) parameter, and nonlinear coefficient, respectively.

This formulation captures the fundamental physical phenomena governing optical signal propagation. Specifically, the first three terms on the left-hand side represent linear effects, including attenuation and chromatic dispersion, whereas the terms on the right-hand side account for nonlinear interactions induced by the intensity-dependent refractive index. The term $\mathrm{i}\gamma|A|^2A$ represents the nonlinear refractive index effects, including SPM, XPM, and FWM. Their magnitude and dynamics depend on both the number of co-propagating signals and their optical power levels. The term $\mathrm{i}\gamma A[\frac{\mathrm{i}}{\omega_0}\frac{\partial(|A|^2A)}{\partial T}]$ accounts for self-steepening (SS), a phenomenon that occurs for short and ultrashort optical pulses. The nonlinear effects discussed above are elastic, as they do not involve energy exchange between the optical signal and the fiber. In contrast, SRS is a non-elastic effect, modeled by the term $\mathrm{i}\gamma[-T_R A\frac{\partial(|A|^2)}{\partial T}]$, with T_R denoting the Raman response time. The last term $g_B Q(z,T)A$ represents the SBS

interaction between the optical field and acoustic phonons in the fiber. The acoustic wave envelope $Q(z,T)$ satisfies $\frac{\partial Q(z,T)}{\partial T} + \Gamma_B Q(z,T) = g_B A(z,T) A_s^*(z,T)$, where g_B is the Brillouin gain coefficient, Γ_B is the acoustic damping constant, and A_s represents the backward-propagating Stokes field.

SBS and SRS can be effectively suppressed by reducing the peak power of the probe pulse. SPM primarily affects the phase evolution of its own signal, whereas FWM becomes significant only under stringent conditions of power and wavelength matching. Consequently, in the ISACoF system, particular attention must be paid to XPM-induced interactions between the communication and sensing channels.

The intensity-dependent refractive index in optical fibers gives rise to XPM, whereby the power fluctuations of co-propagating channels modulate the nonlinear phase of a given wavelength channel. In a multi-channel transmission system with N wavelengths, the XPM-induced nonlinear phase shift of the i-th channel can be expressed as [33]

$$\phi_{NL}^{i} = \gamma L_{\text{eff}} \left(P_i + 2 \sum_{\substack{n=1 \\ n \neq i}}^{N} P_n \right), \tag{8}$$

where $L_{\text{eff}} = \frac{1-\exp(-\alpha L)}{\alpha}$ denotes the effective propagation length, P_i is the input power of the i-th channel, and P_n represents the input powers of the co-propagating channels contributing to XPM. When the probe wavelength is sufficiently detuned from the communication channels, the resulting group-velocity mismatch significantly reduces the temporal overlap of their optical pulses, thereby suppressing XPM-induced nonlinear interactions [34, 35].

3 Experimental setup

The proposed ISACoF system is illustrated in Figure 1. This system seamlessly integrates the OTN with BOTDR/DAS, enabling simultaneous high-capacity data transmission and distributed environmental sensing over a shared optical fiber. The system comprises three main subsystems, including an OTN transmission subsystem, an optical fiber link, and an integrated BOTDR/DAS sensing subsystem. The OTN provides ultra-high-speed data transport, whereas the sensing subsystem exploits Brillouin and Rayleigh scattering mechanisms to achieve distributed measurements of strain, temperature, and vibration along the fiber. This architecture realizes true convergence between communication and sensing functions within a unified optical infrastructure.

Figure 1(a) shows the experimental configuration of the integrated BOTDR/DAS sensing system. A narrow-linewidth laser with a linewidth of 100 Hz, a central wavelength of 1549.972 nm, which corresponds to 193.418 THz, and an output power of 20 mW is used as the light source. The CW laser is divided into two branches using a 50:50 optical coupler (OC1).

In the upper branch, the continuous light is modulated by an AOM with an extinction ratio of 50 dB and a duty cycle of 0.04% to generate pump pulses with a duration of 400 ns, corresponding to a spatial resolution of approximately 40 m, while simultaneously introducing a frequency shift of 20 MHz. A pulse generator drives the AOM to control both the pulse repetition frequency and duty cycle. The modulated pulses are amplified by an erbium-doped fiber amplifier (EDFA1) and then injected into the sensing fiber via a circulator (Cir1). The backscattered light from the sensing fiber is amplified by EDFA2 and subsequently transmitted to Cir2, where it is separated into RBS light and spontaneous Brillouin scattering (SpBS) light using an optical fiber Bragg grating (FBG) filter centered at 1550.06 nm with a bandwidth of 0.08 nm and a reflectivity greater than 95%. The transmitted light is further spectrally filtered by DWDM1 with a channel spacing of 100 GHz and a channel isolation greater than 30 dB to isolate the RBS component, which is then split into orthogonal P- and S-polarized components by a polarization beam splitter (PBS1).

In the lower branch, 50% of the CW light is first split into two paths by an 80:20 OC2. The 20% portion is directed into a polarization beam splitter (PBS2), where it is further separated into orthogonal P- and S-polarized components that serve as reference beams for the DAS system. The P- and S-polarized reference beams from PBS2 are then coherently combined with their corresponding P- and S-polarized RBS from PBS1 through two 50:50 2×2 OC3, generating two independent interference signals. These signals are detected by two balanced photodetectors (BPD1 and BPD2), which have an 80 MHz bandwidth, converting the optical interference into high signal-to-noise ratio (SNR) electrical signals. Finally, the electrical outputs are synchronously sampled by a data acquisition card (DAQ), with a sampling rate of 250 MHz and a vertical resolution of 16 bits, and processed by a computer for digital demodulation and phase reconstruction of the Rayleigh backscattering, high-sensitivity extraction and analysis of distributed vibration information for DAS.

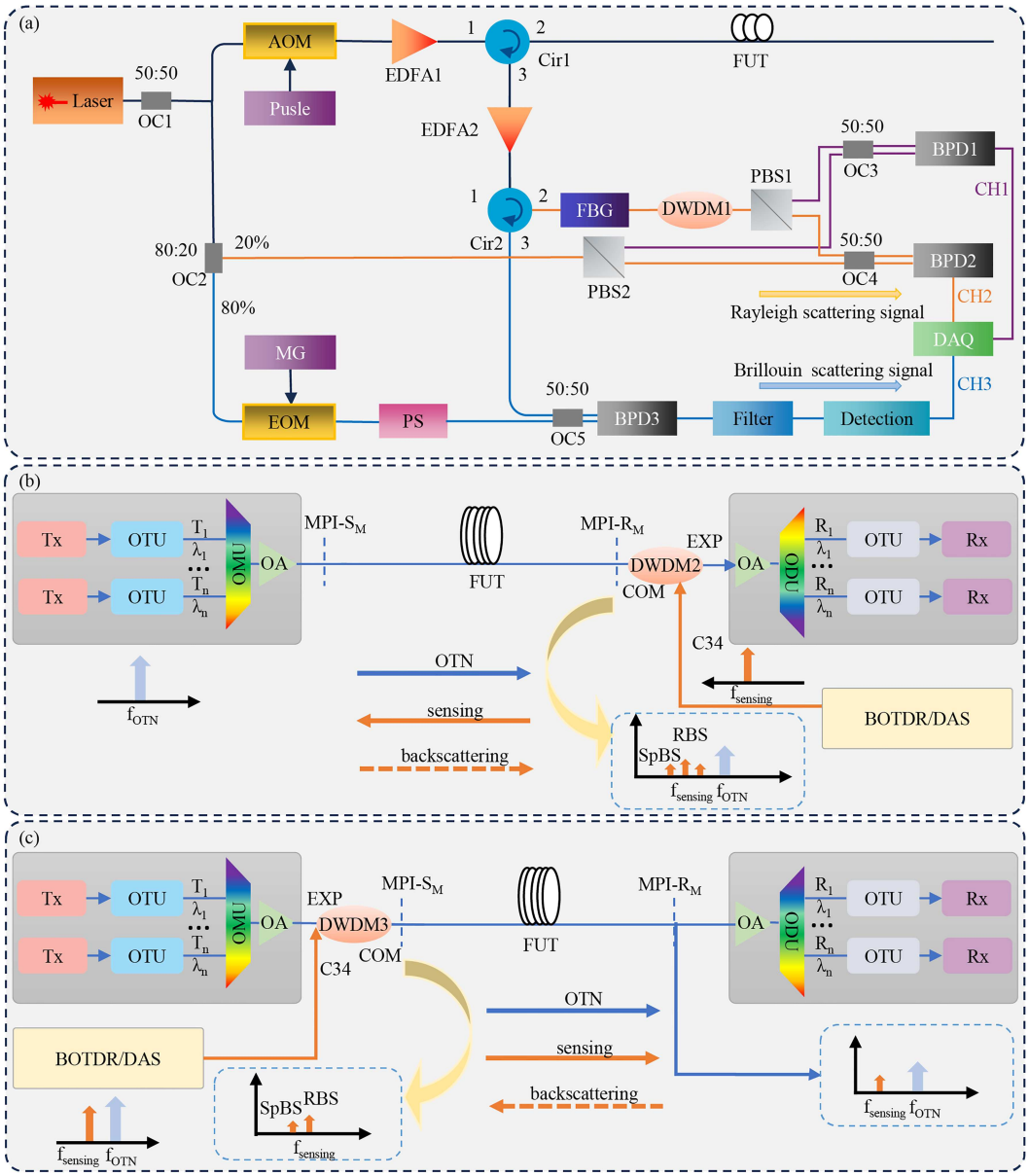

Figure 1 (Color online) Schematic diagram of the ISACoF system. (a) The experimental configuration of the integrated BOTDR/DAS sensing system; (b) the counter-propagating ISACoF system; (c) the forward-propagating ISACoF system.

The system addresses coherent fading, which is a common limitation in coherent-detection-based distributed fiber sensing, through multiple complementary approaches. Spatial sliding averaging is applied along the sensing fiber to suppress random intensity fluctuations caused by coherent fading. Polarization diversity processing is used to reduce polarization-dependent fading and further mitigate coherent fading effects. A rotating vector sum (RVS) algorithm is implemented to coherently combine signals from different polarization states, which improves phase demodulation performance. The combination of spatial averaging, polarization diversity, and RVS processing allows the system to maintain high phase sensitivity, reduce intensity noise, and ensure reliable distributed vibration sensing in practical deployment scenarios.

In the lower branch, 80% of the optical power, serving as the Brillouin reference light, is frequency-modulated by an electro-optic modulator (EOM) driven by a microwave signal swept from 10.55 to 10.85 GHz with 4 MHz steps, generated by a microwave generator (MG). A direct current (DC) power supply is used to adjust the EOM bias voltage, thereby suppressing the carrier component. The polarization state of the Brillouin reference light is then switched by an orthogonal polarization switch (PS) and combined with the backscattered SpBS light via a 2×2 OC5. The fixed-frequency component of the heterodyne Brillouin signal is detected by BPD3 with a bandwidth of 350 MHz. The detected signal is filtered through a band-pass filter (BPF), with a center frequency

of 300 MHz and a bandwidth of 100 MHz, and then processed by an envelope detector (ED). Finally, the envelope signal is recorded by DAQ at a 250 MHz sampling rate for subsequent signal processing.

The communication system adopts a 100 Gbit/s per-channel OTN configuration based on polarization-multiplexed quadrature phase-shift keying (PM-QPSK) coherent detection in the C-band. The transmission employs an 88-channel DWDM scheme with 50 GHz channel spacing, with each wavelength carrying distinct data services independently. The OTN network is implemented on the Alcatel-Lucent 1830 photonic service switch (PSS-32), a platform designed explicitly for multi-layer packet-optical transport, ranging from regional to long-haul applications, and offering ultra-large-scale transmission capacity. Each node is equipped with the S2AD200H 100 G line/tributary integrated module, which consolidates client- and line-side functions into a single unit, reducing both equipment footprint and power consumption. To ensure stable DWDM multiplexing and demultiplexing, the system employs SFD44 (even channels) and SFD44B (odd channels) wavelength multiplexers/demultiplexers, maintaining precise 50 GHz spacing between adjacent optical carriers. This architecture enables high-capacity, spectrally efficient transmission while remaining fully compatible with integrated distributed sensing within the ISACoF framework.

As illustrated in Figures 1(b) and (c), the client signal enters the optical transponder unit (OTU), providing a wavelength-stabilized line-side output, which is multiplexed in the optical multiplexer unit (OMU) and amplified by an optical amplifier (OA), typically implemented using an EDFA before long-haul transmission. At the receiver, the signal is pre-amplified, demultiplexed by the optical demultiplexer unit (ODU), and processed by the OTU for optoelectronic conversion and data regeneration. In the counter-propagating ISACoF architecture shown in Figure 1(b), the BOTDR/DAS sensing pulse is injected via DWDM2, which has the same specifications as DWDM1 at Channel C34, and is combined with the communication signal before the receiver-side amplifier. In the co-propagating configuration shown in Figure 1(c), the sensing pulse is injected through DWDM3, which also has the same specifications as DWDM1 at Channel C34 after the transmitter-side optical amplifier and co-propagates with communication signals. Client interfaces are denoted as T_x and R_x, and standardized optical reference points along the fiber include the transmit multiplex section output, which is marked by MPI-S_M (measurement point interface-sender) at the transmit multiplex section output where the multiplexed signal enters the fiber, and MPI-R_M (measurement point interface-receiver) at the receive multiplex section input, corresponding to the ODU input.

In the ISACoF experiment, the fiber under test consists of four cascaded fiber reels, each approximately 25.25 km in length, resulting in a total span of approximately 101 km. The first three sections are composed of G.654E ultra-low-loss fibers, characterized by Brillouin frequency shifts exceeding 11 GHz. In contrast, the final section employs a G.652D standard single-mode fiber exhibiting a Brillouin frequency shift of approximately 10.85 GHz. This configuration enables a clear distinction of different fiber types along the sensing trace and provides a reference for evaluating the systems spatial discrimination and Brillouin frequency resolution capabilities.

4 Experimental results

4.1 Counter-propagating ISACoF performance

To investigate the impact of signal propagation direction on the performance of ISACoF systems, a counter-propagating configuration for the sensing and communication signals is employed to minimize mutual interference. Specifically, the BOTDR/DAS subsystem interfaces with the OTN receiver via a DWDM module (C34 EXP/COM), enabling counter-propagating transmission of communication and sensing signals, as illustrated in Figure 1(b).

In the BOTDR experiment, pump pulses with a temporal width of 400 ns are launched into the sensing channel, achieving a spatial resolution of approximately 40 m. The peak power of the pump pulses is set to 300 mW, while the double-sideband reference light used for heterodyne detection has an optical power of 400 μW. To enhance the SNR, each measurement is obtained through 10000-fold averaging, resulting in a total acquisition time of approximately 15 min per measurement.

To assess the intrinsic sensing performance of the system, the communication channel is initially deactivated, allowing the sensing subsystem to operate independently. Under these conditions, the maximum effective sensing range reaches 100.977 km, demonstrating the long-haul capability of the sensing subsystem. Subsequently, the communication channel is reactivated while maintaining identical optical power levels and network topology. The communication wavelength is allocated in an adjacent DWDM channel centered at 193.35 THz, ensuring spectral proximity without wavelength overlap.

Figure 2 presents a comparative analysis of the system under two operational modes, namely, sensing-only and ISACoF. As shown in Figure 2(a), the BOTDR subsystem provides the BFS profile along the 100.977-km fiber, while Figure 2(b) depicts the phase-resolved acoustic response of the DAS subsystem over the same span. A

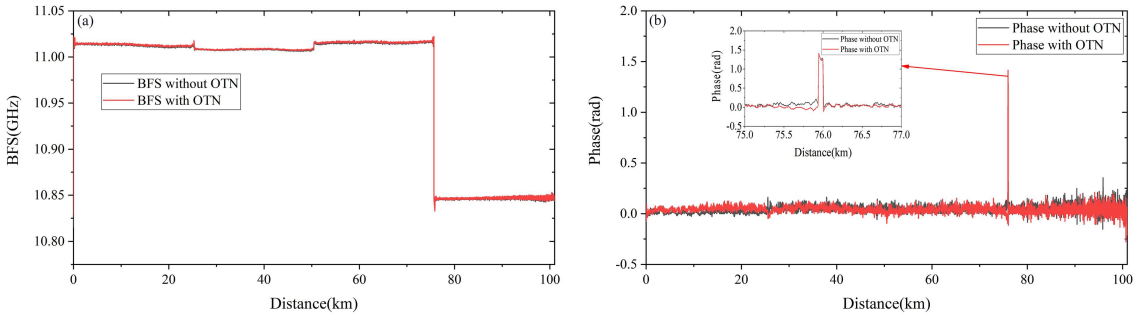

Figure 2 (Color online) Sensing performance in standalone sensing and the ISACoF mode. (a) BOTDR; (b) DAS.

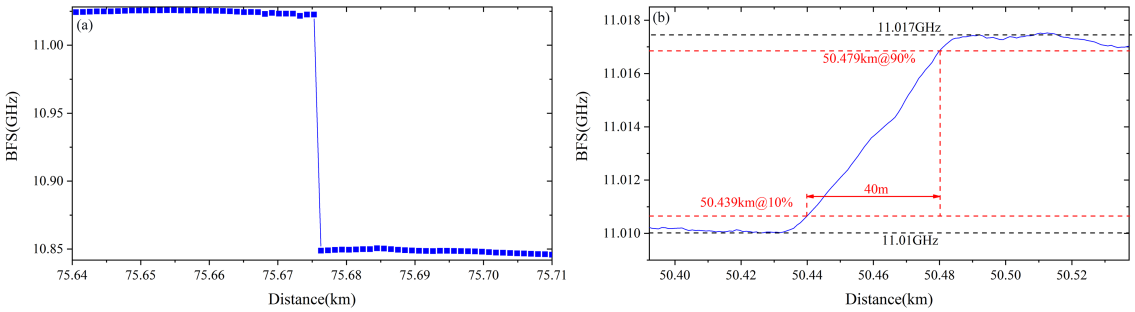

Figure 3 (Color online) Spatial resolution measurement results of the BOTDR subsystem. (a) Result at the 75 km position; (b) result at the 50 km position.

noticeable BFS variation is observed at approximately 75.67 km, which is primarily attributed to the intrinsic differences between the G.654E and G.652D fibers. The splice between these two fiber types introduces a local transition in the BFS profile. Additionally, a 12.28-m piezoelectric transducer (PZT) is installed at this connection point to apply an external sinusoidal vibration for DAS performance evaluation, resulting in an enhanced phase response at this location. The minor differences in phase values between the two operational modes arise from the fact that the presented results correspond to signal snapshots captured at specific time instants, rather than the peak values of the applied sinusoidal excitation. The results demonstrate that the counter-propagating ISACoF configuration effectively isolates the communication and sensing channels, enabling stable distributed measurements while preserving communication quality and minimally affecting sensing accuracy.

To quantitatively evaluate the sensing performance under counter-propagating ISACoF mode, key metrics of the BOTDR/DAS system are systematically compared to elucidate the impact of communication signal injection on the accuracy and stability. To verify the spatial resolution of the BOTDR subsystem, a 25.25 km segment of G.652D fiber is spliced to the end of a 75.67 km G.654E fiber reel. Due to the significantly lower BFS of G.652D fiber (approximately 10.85 GHz) compared with that of G.654E fiber ($>$ 11 GHz), a pronounced BFS transition is observed at the splice point, simulating a step-like BFS change induced by local temperature or strain variation, as illustrated in Figure 3(a). This abrupt transition was intentionally introduced to emulate practical engineering scenarios involving the splicing of different fiber types or localized anomalies such as mechanical damage, material discontinuities, or sudden temperature or strain variations. Owing to the large intrinsic BFS contrast between the two fiber types, the transition occurs within a spatial extent much smaller than the nominal spatial resolution of the BOTDR system. It should be emphasized that this phenomenon represents an apparent step-like response driven by signal amplitude contrast, rather than an actual improvement in the intrinsic spatial resolution. The true spatial resolution of the system remains limited by the pulse-width-defined system response. While such abrupt BFS transitions are valuable for engineering applications, including precise splice localization and detection of large-amplitude localized anomalies, the presence of a substantial BFS discontinuity distorts the Brillouin gain spectrum, rendering this condition unsuitable for high-precision spatial resolution calibration.

Consequently, the splice point at 50.46 km is selected for calibration, where the BFS gradually changes from 11.010 to 11.017 GHz, yielding a total difference of approximately 7 MHz, as shown in Figure 3(b). By defining the 10% (50.439 km) to 90% (50.479 km) range of the BFS transition as the spatial resolution, the BOTDR subsystem achieves a resolution of 40 m.

Under stable temperature and strain conditions, thirty consecutive BFS measurements are performed, and the

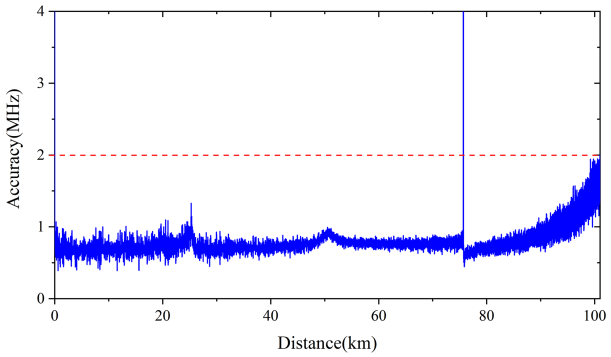

Figure 4 (Color online) Measurement results of the BOTDR subsystem precision.

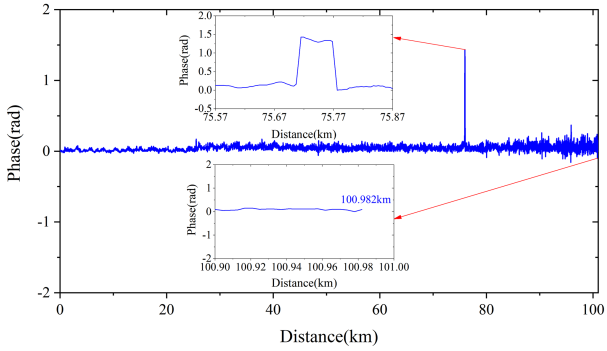

Figure 5 (Color online) Sensing distance measurement results of the DAS subsystem.

standard deviation at each spatial point is calculated to evaluate the intrinsic measurement precision. The results shown in Figure 4 indicate that overall precision along the fiber remains better than 2 MHz. A distinct anomaly around 75.67 km corresponds to the splice between G.654E and G.652D fibers, where the intrinsic BFS difference introduces distortion in the Brillouin gain spectrum, locally deteriorating measurement precision. It is worth noting that the segment preceding the fourth fiber section is located in the inner layers of the wound fiber spool, where environmental perturbations are relatively suppressed. Once the localized spectral distortion is excluded, this region exhibits higher short-term measurement consistency. Detailed analysis indicates that sub-MHz precision is consistently maintained within the 0–90 km range. Beyond 90 km, although the sensing distance is extended by 10 km, the precision deteriorates from about 1 MHz to nearly 2 MHz.

The DAS subsystem enables distributed vibration sensing, relevant for monitoring ice accretion on OPGW cables. Considering that cable vibrations under icing conditions predominantly occur at low frequencies (approximately 1 Hz), a 1 Hz sinusoidal excitation signal with a driving voltage of 3 Vpp is applied to evaluate low-frequency detection performance. Upon injection of optical pulses from the ISACoF system, the DAS subsystem demodulates the phase of backscattered Rayleigh signals, with pulse configuration parameters identical to those used in BOTDR. Time-domain phase traces are recorded, and phase-based sensing distances are calculated, as shown in Figure 5. The phase noise gradually increases with distance, reaching a maximum of approximately 0.37 rad.

The fiber under test spans 100.982 km. A 12 m segment at 75.74 km, corresponding to a fiber junction, is wound on a PZT. Applying a 1 Hz sinusoidal driving voltage of 3 Vpp induces periodic vibration in the fiber segment. As shown in Figure 5, a distinct phase variation is observed from 75.715 to 75.767 km, corresponding to an apparent vibration length of 52 m, with a maximum phase amplitude of 1.43 rad.

It should be noted that the observed vibration length exceeds the physical PZT length of 12 m due to the finite spatial resolution of the DAS system. With an optical pulse width of 400 ns, the nominal spatial resolution is approximately 40 m, so the measured vibration distribution corresponds to the convolution of the true vibration with the systems spatial impulse response.

The DAS subsystem samples at 500 Hz and continuously acquires vibration data for 20 s. The phase signal at the 75.74 km vibration region is presented in Figure 6(a), showing 20 complete sinusoidal cycles consistent with the applied driving signal, with approximately 5 rad phase variation per cycle. Fast Fourier transform (FFT) analysis in Figure 6(b) confirms a dominant spectral peak at 1 Hz, matching the driving signal, with an SNR of 12.1 dB. Figure 6(c) illustrates the spatiotemporal phase distribution over a 70–80 km observation window of 20 s, revealing a distinct periodic variation precisely at the PZT location, further validating low-frequency vibration detection.

To evaluate the phase demodulation accuracy and linear response characteristics of the DAS subsystem, the PZT actuator was driven by a sinusoidal voltage signal, with the peak-to-peak amplitude linearly increased from 1 to 5 Vpp in 0.5 Vpp steps, and the corresponding phase signals were sequentially recorded. The demodulated phase signals exhibit typical sinusoidal waveforms, and the peak-to-peak phase values increase linearly with the applied voltage. For each voltage, the peak-to-peak phase value within one period was calculated, and a linear fit was performed against the applied voltage, as shown in Figure 7. The results demonstrate a strong linear relationship between phase variation and driving voltage across the tested range, confirming the high phase demodulation accuracy and excellent linear response characteristics of the DAS subsystem.

To evaluate the impact of the ISACoF system on transmission performance, the sensing system is operated continuously along the entire fiber link while transmitting a 100 Gbit/s Ethernet (100GE) signal based on PM-QPSK over the shared fiber channel. The communication carrier wavelength was centered at 193.35 THz. During

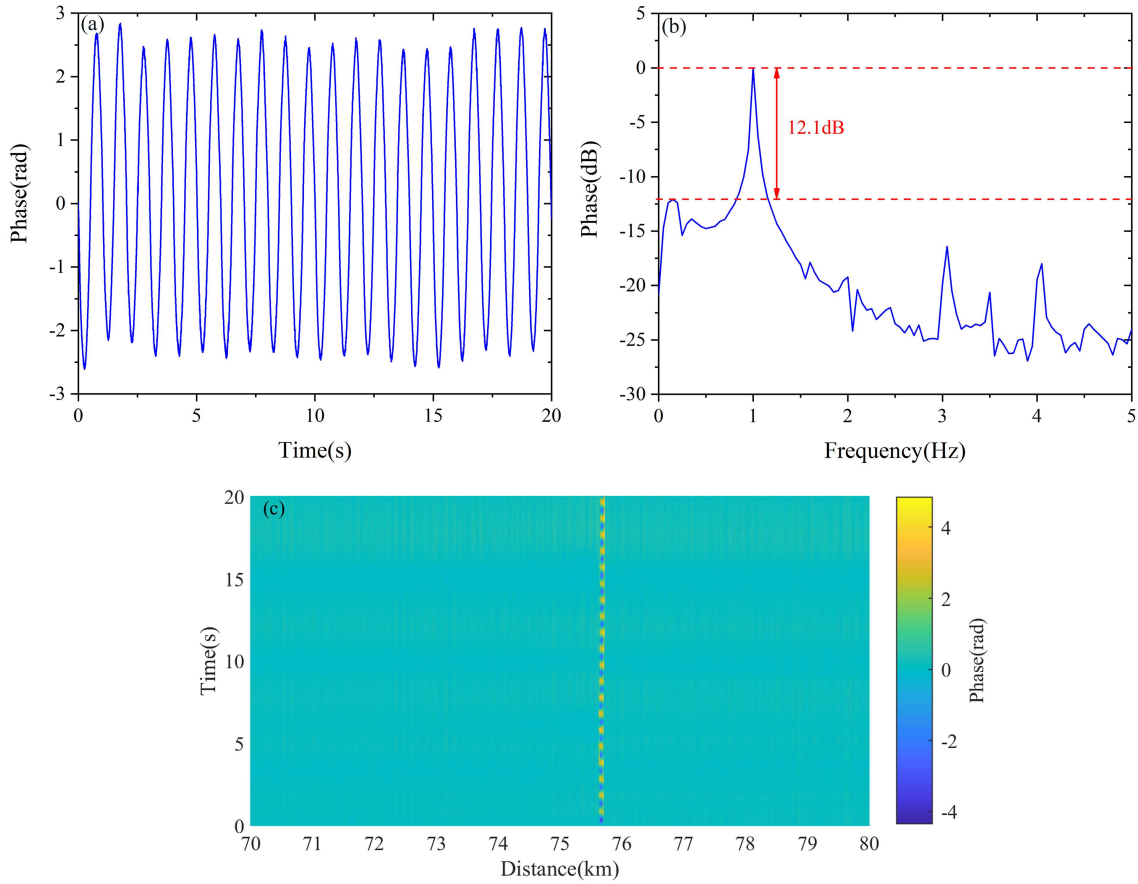

Figure 6 (Color online) Measurement results of PZT-induced vibration using the DAS subsystem at 75 km. (a) Phase result of vibration; (b) frequency result of vibration; (c) phase spatiotemporal distribution map.

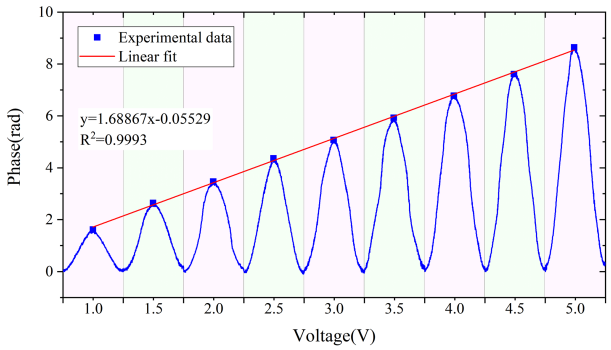

Figure 7 (Color online) Evaluation of the phase linearity of the DAS subsystem.

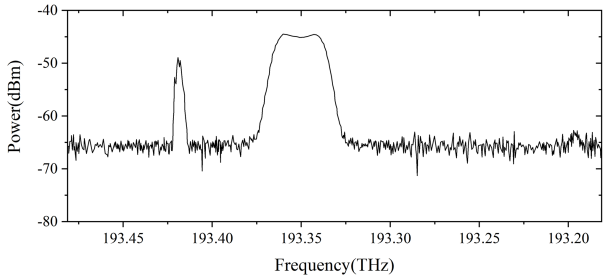

Figure 8 Counter-propagating signal spectrum at the receiver.

15 min of continuous transmission, no bit errors or packet loss were observed, confirming that the system maintains high reliability and stability under counter-propagating sensing conditions. The spectrum of the sensing and communication signals at the counter-propagating receiver is shown in Figure 8.

As illustrated, the receiver spectrum under the counter-propagating configuration presents the simultaneously received communication signal along with the Brillouin and Rayleigh scattering components. Owing to the resolution priority of the observation equipment, two minor peaks can be observed on either side of the Rayleigh scattering spectrum, corresponding to the Brillouin Stokes and anti-Stokes components. By assigning adjacent wavelength channels for communication and sensing, the system successfully separates the high-speed data transmission from the distributed sensing signals, without inducing noticeable distortion in either the communication signal or the scattering spectra. This demonstrates the high spectral integrity and mutual transparency of the co-fiber integration

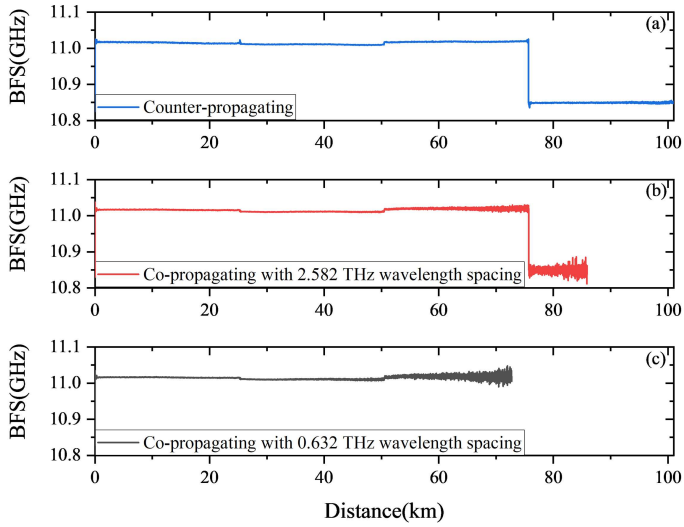

Figure 9 (Color online) Co-propagating sensing distance of BOTDR. (a) Counter-propagating; (b) co-propagating with 2.582 THz wavelength spacing; (c) co-propagating with 0.632 THz wavelength spacing.

scheme under the counter-propagating architecture.

The launched power at MPI-S_M was 0.94 dBm, the received power at MPI-R_M was −26.07 dBm with a span loss of 27.01 dBm, and at R_n, after the ODU and before the OTU input, the long-term received power ranged from 8.00 to 7.96 dBm with an OSNR between 26.83 and 26.95 dB, indicating excellent optical transmission quality with negligible impact from the sensing system. During long-term joint operation of the ISACoF system, the pre-forward error correction (pre-FEC) BER at R_n remains stable between 3.16×10^{-7} and 3.47×10^{-7}, confirming reliable, error-free communication during concurrent distributed sensing, and assuming high-Gaussian noise, the corresponding Q factor can be calculated as

$$Q = \sqrt{2}\,\mathrm{erfc}^{-1}(2\,\mathrm{BER}), \tag{9}$$

where erfc(·) denotes the complementary error function, yielding a Q factor of approximately 5.12–5.13 (linear scale) or 14.2 dB. These results indicate that the ISACoF system introduces negligible degradation in signal quality, with the Q factor remaining virtually unchanged compared with operation without sensing. Furthermore, experimental observations reveal that, by employing the reverse telepathy fusion architecture, the degradation of the Q factor in 100-Gbit/s PM-QPSK communication signals can be limited to less than 0.1 dB, while simultaneously achieving distributed fiber-optic sensing over distances of approximately 100 km without the need for additional optical isolation. Collectively, these findings confirm that the reverse telepathy architecture effectively suppresses nonlinear interactions and minimizes inter-channel interference, providing an efficient and robust solution for integrated long-haul fiber-optic communication and distributed sensing systems.

4.2 Co-propagating ISACoF performance

During co-propagating transmission, the communication BER increases significantly due to XPM. To quantitatively estimate the magnitude of this nonlinear perturbation, we consider the nonlinear coefficient of standard single-mode fiber $\gamma = 1.3\ \mathrm{W^{-1}\,km^{-1}}$ and an effective interaction length of approximately 21 km for a 100 km span with 0.2 dB/km attenuation. For a sensing pulse peak power of 300 mW, the instantaneous XPM-induced phase shift can be approximated as $\Delta\phi_{\mathrm{XPM}} = 2\gamma P_L L_{\mathrm{eff}} = 2 \times 1.3 \times 0.3 \times 21 = 16.38$ rad during pulse overlap. Although this phase perturbation exists only within the pulse duration, in the co-propagating configuration, the interaction extends along the entire fiber span, leading to significant accumulated nonlinear phase distortion on the 100 Gbit/s OTN signal. To mitigate BER degradation in the ISACoF system and ensure standard transmission of communication signals, the peak power of the sensing optical pulse must be reduced. Consequently, the BOTDR sensing distance in the co-propagating operation is shorter than that achieved in the counter-propagating ISACoF configuration, as illustrated in Figure 9.

When the wavelength spacing between the communication and sensing channels is relatively large, with the sensing channel at 193.418 THz and the communication channel at 196 THz, reducing the pump peak power from 300 to 120 mW allows stable communication. Under these conditions, the maximum BOTDR sensing distance

reaches 85.877 km, and considering measurement accuracy, the effective sensing distance is approximately 75 km, as shown in Figure 9(b). For a smaller wavelength spacing, with the sensing channel at 193.418 THz and the communication channel at 194.05 THz, the pump peak power must be further reduced to 50 mW to maintain normal communication. In this case, the maximum BOTDR sensing distance is 72.725 km, with an effective measurement range of approximately 60 km, as shown in Figure 9(c).

In the co-propagating ISACoF configuration, the peak pulse power of the sensing signal does not need to be very high to significantly affect a 100 Gbit/s OTN system. This is because the communication and sensing pulses interact over an extended distance along the fiber, inducing XPM and walk-off, effects that substantially increase the BER of the communication signal. Moreover, the wavelength spacing directly determines the group-velocity mismatch between the two channels. When the wavelength spacing is large, the group velocities differ more significantly, shortening the temporal overlap between the pulses and partially reducing the accumulated XPM. Conversely, when the wavelength spacing decreases, the group velocities become more similar, extending their co-propagation time and increasing the effective nonlinear interaction length, thereby enhancing the XPM-induced phase distortion. To maintain reliable communication and suppress XPM, the peak power of the sensing pulses must be reduced, which in turn limits the effective sensing distance in co-propagating systems.

In contrast, in the counter-propagating ISACoF configuration, the communication signal and sensing pulse collide only within a limited spatial region. The effective nonlinear interaction length is reduced from L_{eff} to approximately $v_g\tau_c$, where τ_c is the pulse collision duration. Since the relative group velocity between counter-propagating waves is approximately $2v_g$, the temporal overlap is significantly shortened compared with the co-propagating case. As a result, the accumulated XPM phase shift is reduced by more than one order of magnitude compared with the co-propagating case. This explains why the measured Q factor penalty remains negligible in the counter-propagating configuration.

Overall, the quantitative analysis confirms that counter-propagating ISACoF mitigates XPM and other nonlinear effects effectively, allowing the simultaneous realization of long-distance distributed sensing and high-speed OTN transmission, where co-propagating ISACoF requires careful power and wavelength spacing management to balance sensing performance and communication integrity. Under the premise of ensuring communication system performance, the measured communication remained stable with OSNR between 25.32 and 25.49 dB and pre-FEC BER between 3.24×10^{-7} and 3.55×10^{-7}.

4.3 Field test results of icing and DC de-icing on OPGW cables

To further evaluate the engineering feasibility of the proposed ISACoF system in actual power grid environments, a field deployment was carried out on an operational ±500 kV extra-high voltage (EHV) transmission line. The ISACoF system was implemented using a DWDM-enabled counter-propagating integration scheme, enabling simultaneous distributed sensing and OTN communication over the same optical fiber without interrupting existing services. The system successfully achieved a sensing range of up to 100 km while maintaining error-free communication, demonstrating its compatibility with long-distance power communication infrastructure.

The integrated sensing system was applied to monitor icing and DC de-icing processes on overhead transmission lines. Distributed temperature measurements along the optical fiber embedded in the OPGW cable were obtained using BOTDR, while DAS was employed to capture vibration signals and extract the natural vibration frequencies of the OPGW cable. Icing thickness was quantitatively inferred from variations in the measured vibration frequency.

The natural vibration frequency of an overhead transmission line can be expressed as

$$f_n = \frac{n}{2l}\sqrt{\frac{T_0}{m}}, \tag{10}$$

where n is the vibration order, f_n is the n-th order natural frequency, l is the OPGW cable span length, T_0 is the horizontal tension, and m is the mass per unit length of the cable. The ice accretion increases the effective mass per unit length, resulting in a decrease in vibration frequency. The ratio of the natural frequency of the iced cable to that of the bare cable can be expressed as [36]

$$\frac{f_{\text{ice}}}{f_0} = \sqrt{\frac{m_0}{m_0 + m_{\text{ice}}}}, \tag{11}$$

where m_0 and m_{ice} denote the mass per unit length of the bare cable and the ice layer, respectively. The ice mass per unit length is approximated as

$$m_{\text{ice}} = \pi\rho_{\text{ice}}[(r_0 + d)^2 - r_0^2], \tag{12}$$

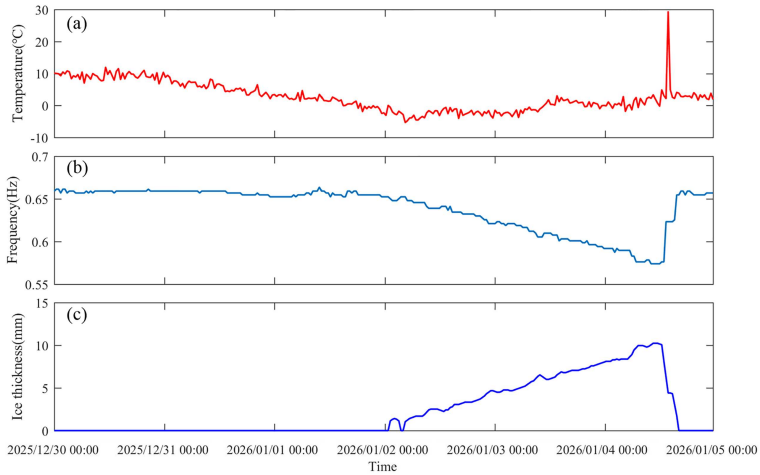

Figure 10 (Color online) Multi-parameter monitoring of the OPGW cable during icing and DC de-icing. (a) Spatiotemporal temperature evolution along the cable measured by BOTDR; (b) vibration frequency obtained by DAS during icing and DC de-icing; (c) temporal evolution of the ice thickness along the cable derived from vibration analysis.

where r_0 is the initial cable radius, d is the ice thickness, and ρ_{ice} is the density of the ice. Substituting this expression into the frequency ratio equation yields an explicit relationship between icing thickness and vibration frequency, allowing real-time estimation of the ice accumulation from DAS measurements,

$$d = \sqrt{\frac{m_0(f_0^2 - f_{\text{ice}}^2)}{\pi\rho_{\text{ice}} f_{\text{ice}}^2} + r_0^2} - r_0. \tag{13}$$

Figure 10 presents the field measurement results at a representative fiber location, illustrating the multi-parameter response of the OPGW cable under icing and DC de-icing conditions. Figure 10(a) depicts the spatiotemporal temperature evolution captured by BOTDR. From December 30, 2025, 00:00 to January 2, 2026, 02:00, the ambient temperature gradually decreased from 10°C to approximately 0°C and remained nearly stable until the initiation of DC de-icing at 14:00 on January 4, 2026. During the de-icing process, the cable temperature rapidly increased to approximately 30°C and subsequently returned to ambient levels after de-icing was completed, demonstrating the system's capability to accurately capture temperature variations associated with icing and melting processes. Figure 10(b) illustrates the vibration frequency measured by DAS. Prior to icing, the cable exhibited a natural frequency of 0.66 Hz. As ice accreted beginning at 02:00 on January 2, 2026, the vibration frequency gradually decreased due to the increased mass loading, reaching a minimum value of 0.58 Hz immediately before the de-icing operation. Following the initiation of DC de-icing, the frequency progressively recovered to its original value of 0.66 Hz, indicating the gradual removal of the ice. Figure 10(c) shows the temporal evolution of the estimated ice thickness derived from the vibration frequency using the theoretical model. The ice thickness increased from zero at the onset of icing to a maximum value of approximately 10 mm prior to de-icing and then decreased to zero during the de-icing process. These results confirm that the proposed ISACoF system enables reliable real-time monitoring of ice accretion and melting. The field validation further demonstrates that the DWDM-based counter-propagating ISACoF architecture supports simultaneous long-distance distributed sensing and high-speed communication on operational EHV transmission lines. In addition, the system provides accurate vibration-based estimation of ice thickness and precise temperature monitoring during de-icing, confirming its practical applicability and engineering feasibility for intelligent monitoring and protection of power transmission infrastructure.

5 Conclusion

In this paper, we proposed and experimentally demonstrated an ISACoF system tailored for next-generation smart power grids. The system employs a dual-heterodyne detection architecture combined with a counter-propagating transmission scheme, enabling cooperative demodulation of BOTDR and DAS signals while maintaining high isolation and stability within the OTN infrastructure. Experimental verification confirms that the system achieves long-distance co-fiber operation over 100 km, supporting simultaneous high-speed data transmission and distributed sensing of temperature, strain, and vibration.

Experimental results show that during 100 Gbit/s PM-QPSK transmission, the OSNR remains above 23 dB and the BER stays on the order of 10^{-7}, with no noticeable degradation in communication performance. The BOTDR subsystem achieves a spatial resolution of 40 m and a BFS accuracy of 2 MHz, while the DAS subsystem maintains a phase noise level of only 0.37 rad across 100 km, enabling detection of low-frequency vibrations down to 1 Hz. Furthermore, field deployment on an operational 500 kV transmission line demonstrates the practical capability of the proposed system for power grid monitoring, including accurate prediction of a 10 mm ice layer and continuous temperature tracking during the DC de-icing process, with the maximum temperature reaching 30°C. These results validate the high compatibility, low interference, and mutual transparency between communication and distributed sensing subsystems under co-fiber operation.

It should be noted that for co-propagating integration, suppression of nonlinear crosstalk, such as XPM, typically requires reducing the sensing signal power or increasing the wavelength spacing between the sensing and communication channels. However, these adjustments inevitably degrade either the communication power budget or the sensing SNR, preventing the realization of optimal performance for both functionalities. Therefore, the counter-propagating integration scheme adopted in this work provides a more balanced and practical approach, offering enhanced system stability and reduced nonlinear interference.

In summary, the proposed ISACoF system lays a solid technological foundation for realizing intelligent, self-sensing, and self-healing optical transport networks in future smart grids. The demonstrated approach offers both theoretical insight and experimental evidence toward multifunctional optical infrastructures that seamlessly integrate communication and distributed sensing.

Acknowledgements This work was supported by National Key Research and Development Program of China (Grant No. 2023YFF0715803), Postdoctoral Scientific Research Development Fund of Heilongjiang Province (Grant No. LBH-Q21092), National Key Laboratory of Laser Spatial Information Foundation (Grant No. LSI2024WDZC003), and National Natural Science Foundation of China (Grant No. 62205297).

References

1 ITU-T. Architecture of optical transport networks. ITU-T Recommendation G.872, 2021
2 Fu R, Wang L. Research on control and management of smart grid optical network based on optical transmission control protocol (OTN) technology. Thermal Sci Eng Prog, 2024, 53: 102763
3 Lu P, Lalam N, Badar M, et al. Distributed optical fiber sensing: review and perspective. Appl Phys Rev, 2019, 6: 041302
4 Bao X, Chen L. Recent progress in distributed fiber optic sensors. Sensors, 2012, 12: 8601–8639
5 Wan A C, Wu Y Q, Zhang S, et al. Co-channel multiplexing for Rayleigh-scattering-based information systems. Sci China Inf Sci, 2025, 68: 182304
6 Xia M, Tang X, Wang Y, et al. OPGW positioning and early warning method based on a Brillouin distributed optical fiber sensor and machine learning. Appl Opt, 2023, 62: 1557–1566
7 Yao Y, Wang R, Ding H, et al. A fast and accurate mapping method for an OPGW tower based on hybrid distributed optical fiber sensing. Sensors, 2024, 24: 5629
8 Luo Y, Gao C, Wang D, et al. Predictive model for sag and load on overhead transmission lines based on local deformation of transmission lines. Electric Power Syst Res, 2023, 214: 108811
9 Hao Y, Liu N, Kun Y, et al. Online ice-coating monitoring research on overhead transmission lines with Brillouin optical time domain reflectometry. Optical Fiber Tech, 2020, 60: 102339
10 Li X, Zhou M, Luo Y, et al. Insulation reconstruction for OPGW DC De-Icing and its influence on lightning protection and energy conservation. Energies, 2018, 11: 2441
11 Lu L, Liang Y, Li B, et al. Experimental study on location of lightning stroke on OPGW by means of a distributed optical fiber temperature sensor. Optics Laser Tech, 2015, 65: 79–82
12 Xu Z, Song S, Zhao L, et al. Research on influencing factors of OPGW icing monitoring method based on phase difference between temperature curves. IEEE Trans Power Deliver, 2025, 40: 2005–2016
13 Sun J, Zhang Z, Li Y, et al. Distributed transmission line ice-coating recognition system based on BOTDR temperature monitoring. J Lightwave Technol, 2021, 39: 3967–3973
14 Shao L, Zhang J, Chen X, et al. Artificial intelligence-driven distributed acoustic sensing technology and engineering application. PhotoniX, 2025, 6: 4
15 Canudo J, Sevillano P, Iranzo A, et al. Simultaneous structural monitoring over optical ground wire and optical phase conductor via chirped-pulse phase-sensitive optical time-domain reflectometry. Sensors, 2024, 24: 7388
16 Ding Z W, Zhang X P, Zou N M, et al. Phi-OTDR based on-line monitoring of overhead power transmission line. J Lightwave Technol, 2021, 39: 5163–5169
17 Zhang J F, Lu W D, Xing C W, et al. Intelligent integrated sensing and communication: a survey. Sci China Inf Sci, 2025, 68: 131301
18 Marra G, Clivati C, Luckett R, et al. Ultrastable laser interferometry for earthquake detection with terrestrial and submarine cables. Science, 2018, 361: 486–490
19 Zhan Z, Cantono M, Kamalov V, et al. Optical polarization-based seismic and water wave sensing on transoceanic cables. Science, 2021, 371: 931–936
20 Mecozzi A, Cantono M, Castellanos J C, et al. Polarization sensing using submarine optical cables. Optica, 2021, 8: 788–795
21 Cantono M, Marra G, Kamalov V, et al. Seismic sensing in submarine fiber cables. In: Proceedings of the 2021 European Conference on Optical Communication (ECOC). Bordeaux: IEEE, 2021. 1–3
22 Ip E, Huang Y K, Wellbrock G, et al. Vibration detection and localization using modified digital coherent telecom transponders. J Lightwave Technol, 2022, 40: 1472–1482
23 Andrenacci L, Pilori D, Pellegrini S, et al. Comparison between phase and polarization sensing using coherent transceivers over deployed metro fibers. In: Proceedings of the 2024 Optical Fiber Communications Conference and Exhibition (OFC), San Diego, 2024. 1–3
24 Kong W, Liu F, Zhu G, et al. Localization enhancement of forward-transmission distributed vibration sensors using phase differentiation endpoint amplification. IEEE Sens J, 2024, 24: 17669–17676
25 He H, Jiang L, Pan Y, et al. Integrated sensing and communication in an optical fibre. Light Sci Appl, 2023, 12: 25
26 Wellbrock G A, Xia T J, Huang M F, et al. First field trial of sensing vehicle speed, density, and road conditions by using fiber carrying high speed data. In: Proceedings of 2019 Optical Fiber Communications Conference and Exhibition (OFC), San Diego, 2019. 1–3
27 Huang M F, Ji P, Wang T, et al. First field trial of distributed fiber optical sensing and high-speed communication over an operational telecom network. J Lightwave Technol, 2020, 38: 75–81

28 Jia Z S, Campos L A, Xu M, et al. Experimental coexistence investigation of distributed acoustic sensing and coherent communication systems. In: Proceedings of the 2021 Optical Fiber Communications Conference and Exhibition (OFC), San Francisco, 2021. 1–3
29 Cao X L, Li Z Y, Li X H, et al. Intelligent submarine environmental monitoring based on fiber-optic integrated sensing and communication system. Sci China Inf Sci, 2026, 69: 160303
30 Wang J C, Liu M Q, Lu L W, et al. Simulation and experimental studies of DWDM nonlinear phase polarization power crosstalk between DFOS and communication channels in 27.6-Tb/s 800ZR metro network. ArXiv:2505.12797
31 Xie C. Impact of nonlinear and polarization effects in coherent systems. Opt Express, 2011, 19: B915
32 Reis J D, Teixeira A L. Cross-phase modulation impact on coherent optical 16 QAM-WDM transmission systems. Micro Opt Tech Lett, 2011, 53: 633–636
33 Singh S P, Singh N. Nonlinear effects in optical fibers: origin, management and applications. Prog Electromagn Res, 2007, 73: 249–275
34 Agrawal G P, Baldeck P L, Alfano R R. Temporal and spectral effects of cross-phase modulation on copropagating ultrashort pulses in optical fibers. Phys Rev A, 1989, 40: 5063–5072
35 Kassegne D, Singh S, Ouro-Djobo S S, et al. Influence of nonlinear effects on 6.4 Tb/s dual polarization quadrature phase shift keying modulated dense wavelength division multiplexed system. Int J Communication, 2019, 32: e4021
36 Ding Z W, Zhang X P, Zou N M, et al. Phi-OTDR based on-line monitoring of overhead power transmission line. J Lightwave Technol, 2021, 39: 5163–5169